3D Poro-Thermo-Elastic Numerical Model
for Analysing Pressure-Transient Response to Improve the Characterization
of Naturally Fractured Geothermal Reservoirs

**Reda Abdel Azim[1], Nima Gholizadeh Doonechaly[1], Sheik S. Rahman[1],
Stephen Tyson[2], and Klaus Regenauer-Lieb[1]**

**[1]The University of New South Wales, Sydney, Australia
[2]The University of Queensland, Brisbane, Australia**

ABSTRACT

This paper presents an innovative three-dimensional fully-coupled poro-thermo-elastic numerical model for simulation of pressure-transient response of naturally fractured reservoirs. One of the main purposes of the approach is to improve the reservoir characterization by reducing the uncertainties associated with sub-surface fracture mapping. In this paper an innovative methodology of tracking the fracture backbone in microseismic cloud events is used to generate the subsurface map. The coupled fluid-flow and heat-transfer model is based on a hybrid of the single-continuum and the discrete-fracture approach.

The 3D-numerical simulation model is validated against an analytical pressure-transient solution for a dual-porosity system and then applied to the Habanero enhanced geothermal system (EGS) in Central Australia. The results of the study also show that the simulated pressure change and pressure derivatives agree well with the field production data, which makes the innovative approach of tracking of fracture backbone in microseismic cloud events and simulation of pressure derivatives highly effective in predicting the fracture network along with its inherent properties.

Introduction

Numerous methodologies have been proposed in the literature to simulate flow of slightly compressible fluid in naturally fractured reservoirs. An example is the dual-porosity concept which was proposed by Barenblatt and others (1960) to simulate flow of single-phase fluid in naturally fractured rocks (Barenblatt et al. 1960, Barenblatt and Zheltov 1960). Their models were based on the two overlapping continua of a reservoir: fractures and matrix. Warren and Root (1966) simplified the fluid flow in fractured reservoirs by considering fractures as a series of evenly spaced parallelepipeds. This means, fractures provide the main flow paths while the matrix acts as a sink/source (mass) to the fractures (Warren and Root 1963). In dual-porosity approach, the fluid transfer between the fractures and the matrix is defined based on the specific transfer functions (Beckner et al. 1987). Carlson (2003) improved the matrix-fracture interface by introducing a new transfer function, however, the dual-porosity model can only be used for the systems with small contrast between the fracture and matrix permeabilities.

Kuchuk and Habashy (1997) used the dual porosity model to simulate fluid flow in multiple faults and fractures and studied transient pressure behaviour. In this study the authors considered both finite and infinite conductivities but the well did not have interaction with fractures or faults. Although the model had significant limitations results showed that fractures are the dominant contributors to the pressure-transient behaviour in such reservoirs. Wei et al. (1998) used a dual porosity model to study the pressure-transient derivative in both continuous and discrete fracture networks. Authors concluded that dual porosity models do not adequately describe the behaviour of the fractured reservoirs.

Bogdanov et al. (2003) presented a finite volume technique, while Casabianca et al. (2007) used an integrated interpretation methodology to simulate single phase fluid flow in discrete fractures and studied pressure derivative behaviour. Morton et al. (2012), on the other hand developed an analytical-element method to simulate the pressure-transient response of a reservoir with arbitrarily-oriented vertical fractures. Biryukov and Kuchuk (2012) presented a discrete conductive fracture model to investigate flow regimes for different fracture patterns. In all these studies authors have not considered the effects of geomechanics and flow properties are approximated.

In this study a hybrid methodology, which combines the single-continuum and the discrete-fracture approaches, is used to simulate fluid flow in a poro-thermo-elastic environment and study pressure transient behavior of randomly oriented fractured reservoirs.. The authors have used Habanero enhanced geothermal system as case study. In the proposed methodology a threshold value for fracture length is defined. Fractures, which are smaller than the threshold value, are used to generate the grid based permeability tensor. The reservoir domain is divided into a number of grid blocks,

and the fluid-flow simulation is carried out by using the single-continuum approach in the nominated blocks. Fractures, which are longer than the threshold value, are explicitly discretized in the domain using appropriate elements and the fluid-flow is modeled using the discrete fracture approach. Such an approach provides a more accurate and realistic framework to study the effect of long fractures on the fluid-flow in fractured medium.

First an analytical solution for pressure derivative of a dual porosity system is used to validate the numerical model. Then the numerical model is used to generate pressure derivatives and compared with the well test data from the Habanero enhanced geothermal reservoir.

Subsurface Mapping of Fracture Network Backbones

Numerous methodologies have been proposed in the literature to generate the subsurface fracture map of the reservoirs. Comprehensive discrete fracture network (DFN) models provide an understanding of the reservoir make up and help select the best locations for production wells, study the response of natural fractures under induced stimulation pressure and develop optimum production methods to maximize recovery (Nelson and Laubach 1994, Gholizadeh Doonechaly and Rahman 2012). Micro-seismic events can be used as a powerful tool to determine the geographical extent of the reservoir, the hydraulic performance, stimulation response of the reservoir (Koh et al. 2010, Gholizadeh Doonechaly et al. 2012, Gholizadeh Doonechaly et al. 2012, Doonechaly et al. 2013) and fracture network properties (Alghalandis et al. 2013). Microseismic events recorded during water injection occur primarily at the tips of the fractures (Warpinski et al. 2004). Assuming that all the recorded events are tip-events, a fracture network backbone may be computed using a Euclidean Minimum Spanning Tree (EMST) algorithm (March et al. 2010). Figure 1 show the complete Fracture Network generated in this study by using EMST in a plan view. Details of this fracture network are shown in figures 2 and 3. Figure 4 shows the same network detail as Figure 3 with the addition of the location of the microseismic events colored using their recorded magnitude.

To estimate the fracture planes the length of each segment in the fracture network backbone was computed and a fracture height was assigned based on a height to length ratio. The initial value of this ratio was set to be 0.1, though this is a parameter that can be adjusted. Dip angles for the fractures were assigned stochastically based upon the mean and variance of dip-angle distributions measured in similar environments from image logs. This process creates a complete 3D backbone of the fracture network linking each of the microseismic events.

The assumption that all microseismic events that are recorded during pumping occur at the tips of the existing fracture network is not necessarily correct. Figure 5 shows the microseismic events recorded at the Habanero site up to and including 12 September 2005. There are clearly multiple clusters of data. The events in the south west are those associated with pumping in Habanero #2 which commenced on 7 August 2005. The large cluster in the north east is associated with pumping in Habanero #1 which started on 6 September but stopped for 48 hours on September 8 due to a pump malfunction. A time-stepped EMST algorithm is

being developed to add events to an existing EMST which would result in a more accurate fracture backbone. Figure 5 shows more than two clusters of events. There are individual events between the two well-induced clusters, and there is another cluster between the two wells. These individual points and the smaller cluster between the two wells, could be due to extension of the existing fracture network from Habanero #1 or Habanero #2, or it could be induced seismicity due to the changing stress conditions resulting from pumping into the two wells. The fracture network that is created would be different for these two different alternatives, and a scenario-based algorithm for the computation of an accurate fracture network backbone is currently being developed. This algorithm uses additional information from the microseismic signatures to classify microseismic events as a pre-processing step to the construction of the EMST.
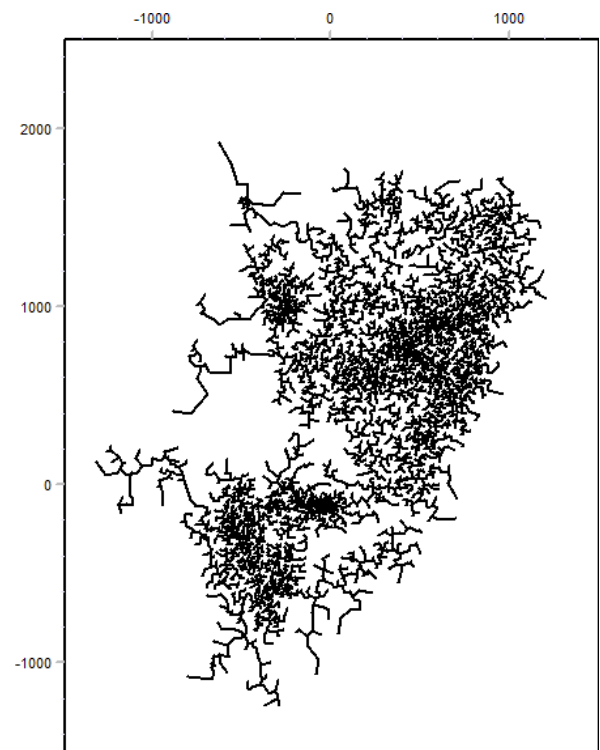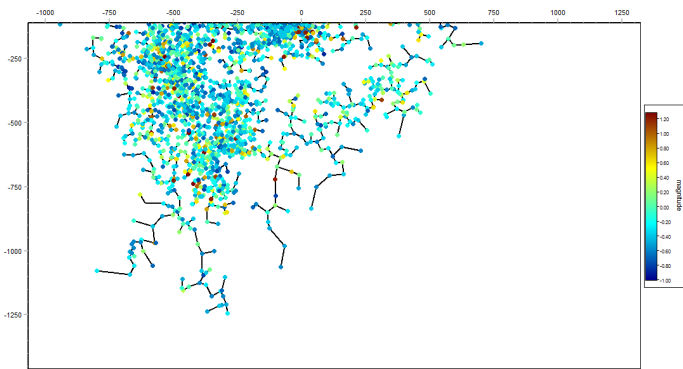

Figure 1. Complete fracture network for the Habanero field generated in this study by the EMST algorithm.
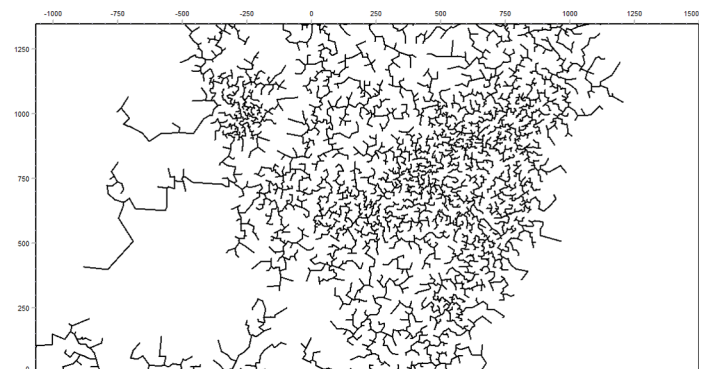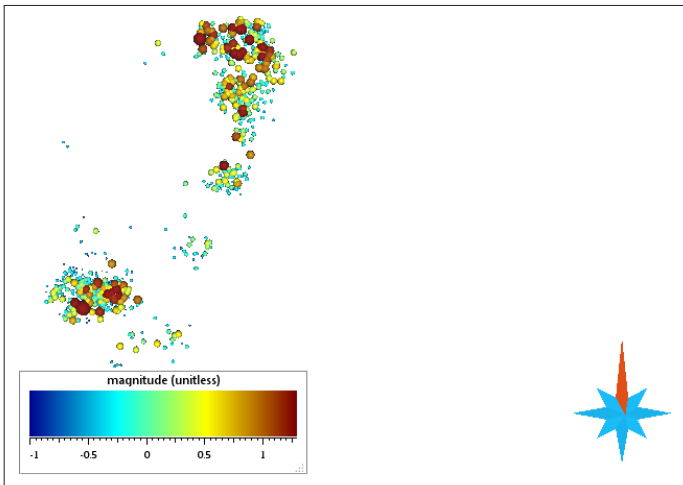

Figure 2. Fracture network detail for the Habanero field generated in this study by the EMST algorithm.
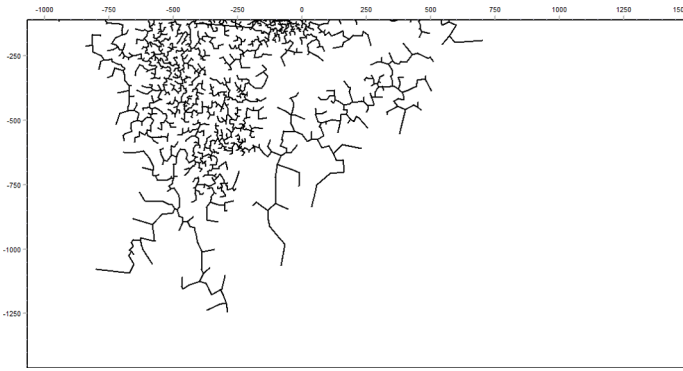
Figure 3. Fracture network detail of the lower part of the Habanero field generated by EMST algorithm.

Figure 4. Fracture network detail showing event magnitude for the lower part of the Habanero geothermal field.

Figure 5. Microseismic events recorded until to 12 September 2005.

Poro-Thermo-Elastic Simulation

The momentum balance equation for the linear elastic deformations can be written as:

$$\nabla \cdot \sigma + \rho g = 0 \tag{1}$$

where ρ is the density of the porous medium which can be written as Eq. (2) and g is the gravity constant.

$$\rho = \varphi \rho_l + (1-\varphi)\rho_s \tag{2}$$

Also Eq. (1) can be written in terms of effective stress as follows:

$$\nabla \cdot (\sigma' - pI) + \rho g = 0 \tag{3}$$

where σ' is the effective stress, p is the pore pressure and I is the identity matrix. The constitutive equation for the stress-strain relationship in a non-isothermal environment can be written as in Eq.(4) and with few modifications can be written as in Eq. (5).

$$d\sigma' = D(d\varepsilon - d\varepsilon^T) \tag{4}$$

$$\sigma' = C(\varepsilon - \alpha_T \Delta T \times I) \tag{5}$$

where D is the operator matrix (Zienkiewicz 2000), ε^T is the thermal strain, ε is the total strain, α_T is the thermal expansion coefficient, ΔT is the temperature difference, and C is the fourth order material tensor as shown in Eq. (6).

$$C = \lambda \delta_{ij}\delta_{kl} + 2G\delta_{ik}\delta_{jl} \tag{6}$$

In Eq. (6), δ is the Kronecker delta function, G is the shear modulus of elasticity, and λ is the Lame coefficient. Also the constitutive equation for the total strain-displacement relationship is defined as follows:

$$\varepsilon = \frac{1}{2}(\nabla u + (\nabla u)^T) \tag{7}$$

The mass-balance equation for the fluid phase in a deformable non-isothermal porous medium can be written as follows:

$$S_s \frac{\partial p}{\partial t} + \nabla \cdot q + \nabla \cdot (\frac{\partial u}{\partial t}) - \alpha_T \frac{\partial T}{\partial t} = Q \tag{8}$$

where S is the specific storage which is defined as shown in Eq. (9), p is the pore fluid pressure, T is the temperature, α_T is the thermal expansion coefficient, q is the fluid flux and Q is the sink/source term.

$$S = (\frac{1-\varphi}{K_s}) + (\frac{\varphi}{K_l}) \tag{9}$$

Also the fluid flux term (q) in Eq. (8) can be described by using Darcy's flow equation as follows:

$$q = -\frac{k}{\mu}(\nabla p - \rho g) \tag{10}$$

Introducing Eqs. (10) and (9) into Eq. (8) results in the following equation as the general mass conservation equation for a fully saturated (single phase) deforming porous medium in a non-isothermal environment:

$$\left[(\frac{1-\varphi}{K_s}) + (\frac{\varphi}{K_l})\right]\frac{\partial p}{\partial t} + \nabla \cdot (\frac{\partial u}{\partial t}) - \alpha_T \frac{\partial T}{\partial t} +$$

$$\nabla^T \left[-\frac{k}{\mu}(\nabla p - \rho g)\right] = 0 \tag{11}$$

In Eq. (11), α_T is the thermal expansion coefficient of the medium and can be obtained using the following equation:

$$\alpha_T = (1-\varphi)\alpha_{T_{solid}} + \varphi\alpha_{T_{liquid}} \tag{12}$$

where φ is the orosity of the medium, $\alpha_{T_{solid}}$ is the thermal expansion coefficient of the solid phase, and $\alpha_{T_{liquid}}$ is the thermal expansion coefficient of the liquid phase.

The energy-balance equation for a saturated porous medium can be written as:

$$(\rho c_p)_{eff} \frac{\partial T}{\partial t} + \nabla . q T = Q_T \tag{13}$$

where $(\rho c_p)_{eff}$ is the effective heat storage of the porous medium which is defined in Eq. (14), q is the heat flux, and Q_T is the heat sink/source term.

$$(\rho c_p)_{eff} = \varphi(c_p \rho)_{liquid} + (1-\varphi)(c_p \rho)_{solid} \tag{14}$$

Also, both conduction and convection heat transfers are considered in this study based on which the heat flux term in Eq. (13) can be written as:

$$q T = -\lambda_{eff} \nabla T + (c_p \rho)_{liquid} v \cdot T \tag{15}$$

where λ_{eff} is the effective heat conductivity of the porous medium which can be defined as Eq. (16) and v is the velocity of the fluid. Also, the first term on the right-hand side of Eq. (15) is the conduction term, and the second term is the convective heat-transfer term.

$$\lambda_{eff} = \varphi \lambda_{liquid} + (1-\varphi)\lambda_{solid} \tag{16}$$

By introducing the Darcy's law into Eq. (15) the general energy conservation equation for a fully saturated single phase deformable porous medium in a non-isothermal framework can be written as:

$$(\rho c_p)_{eff} \frac{\partial T}{\partial t} + \left[(c_p \rho)_{liquid} \times \frac{k}{\mu} \times (-\nabla p + \rho g) \right] \cdot$$
$$\nabla T - \nabla^T (\lambda_{eff} \nabla T) = Q \tag{17}$$

In order to discretise the above-mentioned mass-, momentum- and energy-conservation equations, the weighted residual method and the Green's theorem are applied (Bathe 1996). As mentioned before, the finite-element method is used in this study for the purpose of numerical simulation purpose. Therefore the state variables (namely: displacement, pore pressure and temperature) are defined using proper shape functions as:

$$u = N_u \overline{u} \tag{18}$$

$$p = N_p \overline{p} \tag{19}$$

$$T = N_T \overline{T} \tag{20}$$

where, N is the corresponding shape function and $\overline{u}$, $\overline{p}$ and $\overline{T}$ are the nodal values of the corresponding state variable. By applying the Galerkin's method and replacing the weighting functions by the corresponding variables' shape functions, the weak form of the conservation equations can be written as follows (Watanabe et a. 2010 Koh et al. 2011, Gholizadeh Doonechaly et al. 2012, Watanabe 2012):

$$\int_\Omega w S_s \frac{\partial p}{\partial t} d\Omega + \int_\Omega w^T \alpha \nabla \cdot \frac{\partial u}{\partial t} d\Omega + \int_\Omega w \beta \frac{\partial T}{\partial t} - \int_\Omega \nabla w^T \cdot q_H d\Omega +$$
$$\int_{\Gamma_H^q} w(q_H \cdot n) d\Gamma - \int_\Omega w Q_H d\Omega = 0 \tag{21}$$

$$\int_{\Gamma_d} w b_m S_s \frac{\partial p}{\partial t} d\Gamma + \int_{\Gamma_d} w \alpha \frac{\partial b_m}{\partial t} d\Gamma + \int_{\Gamma_d} w \beta \frac{\partial T}{\partial t} d\Gamma - \int_{\Gamma_d} \nabla w^T \cdot (b_h q_H) d\Omega$$
$$+ \int_{\Gamma_H^q} w b_h (q_H \cdot n) d\Gamma + \int_{\Gamma_d} w q_H^+ d\Gamma + \int_{\Gamma_d} w q_H^- d\Gamma = 0 \tag{22}$$

$$\int_\Omega w c_p \rho \frac{\partial T}{\partial t} d\Omega + \int_\Omega w c_p \rho q_H \cdot \nabla T d\Omega - \int_\Omega \nabla w^T \cdot (-\lambda \nabla T) d\Omega$$
$$+ \int_{\Gamma_T^q} w(-\lambda \nabla T \cdot n) d\Gamma - \int_\Omega w^T Q_T d\Omega = 0 \tag{23}$$

$$\int_{\Gamma_d} w b_m c_p^l \rho^l \frac{\partial T}{\partial t} d\Gamma + \int_{\Gamma_d} w c_p^l \rho^l b_h q_H \cdot \nabla T d\Gamma - \int_{\Gamma_d} \nabla w^T \cdot (-b_m \lambda^l \nabla T) d\Gamma$$
$$+ \int_{\Gamma_T^q} w(-b_m \lambda^l \nabla T \cdot n) d\Gamma + \int_{\Gamma_d} w q_T^+ d\Gamma + \int_{\Gamma_d} q_T^- d\Gamma = 0 \tag{24}$$

$$\int_\Omega \nabla^s w^T \cdot (\sigma' - \alpha p I) d\Omega - \int_\Omega w^T \cdot \rho g d\Omega - \int_{\Gamma_t} w^T \cdot \overline{t} d\Gamma - \int_{\Gamma_d} w^{+T} \cdot t_d^+ d\Gamma$$
$$- \int w^{-T} \cdot t_d^- d\Gamma = 0 \tag{25}$$

where w is the test function, Ω is the model domain, Γ is the domain boundary, t is the traction vector and d is the fracture plane.

Effective Permeability Tensor Calculations

Three-dimensional flow equations used for permeability-tensor calculations are given by Darcy's law and continuity equation as:

$$\begin{Bmatrix} u_x \\ u_y \\ u_z \end{Bmatrix} = \begin{bmatrix} k_{xx} & k_{xy} & k_{xz} \\ k_{yx} & k_{yy} & k_{yz} \\ k_{zx} & k_{zy} & k_{zz} \end{bmatrix} \begin{Bmatrix} \dfrac{\partial p}{\partial x} \\ \dfrac{\partial p}{\partial y} \\ \dfrac{\partial p}{\partial z} \end{Bmatrix} \tag{26}$$

$$\nabla . u = 0.0 \tag{27}$$

where u is the fluid velocity vector. Periodic boundary conditions are required for solving all elements of permeability tensor in Eq. (26). Periodic boundary condition was proposed by Durlofsky (1991) by assuming a constant pressure gradient along one direction with zero pressure gradients in all other directions, as shown in Eqs. (28), (29) and (30) shows.

$$v_x = -k_{xx} \frac{\partial p}{\partial x} - k_{xy} \frac{\partial p}{\partial y} - k_{xz} \frac{\partial p}{\partial z} \tag{28}$$
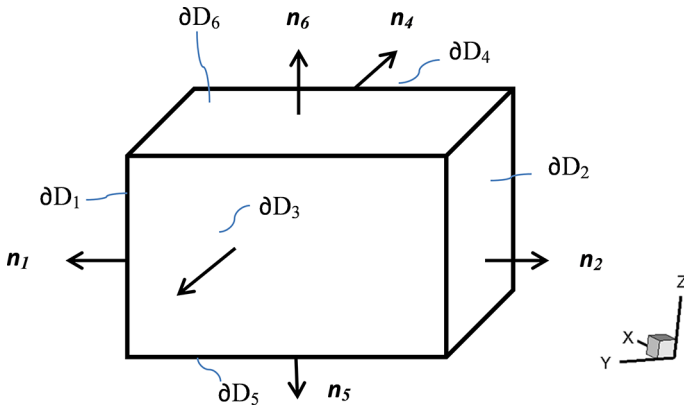
$$v_y = -k_{yx} \frac{\partial p}{\partial x} - k_{yy} \frac{\partial p}{\partial y} - k_{yz} \frac{\partial p}{\partial z} \tag{29}$$

$$v_z = -k_{zx} \frac{\partial p}{\partial x} - k_{zy} \frac{\partial p}{\partial y} - k_{zz} \frac{\partial p}{\partial z} \tag{30}$$

Pressure and flux boundaries are specified in Eq. (31) to Eq. (36). By specifying a zero pressure gradient along the other faces $\left(\frac{\partial p}{\partial y} = 0.0, \frac{\partial p}{\partial z} = 0.0 \right)$ three elements of permeability tensor can be determined as follows:

Figure 6. Periodic boundary conditions used to calculate elements of permeability tensor in a three-dimensional space by using single-phase flow model.

P (y, x=0, z) = P (y, x=1, z)   on ∂D_3 and ∂D_4 (31)

u (y, x=0, z)•$\boldsymbol{n_3}$ = -u (y, x=1, z)•$\boldsymbol{n_4}$ on ∂D_3 and ∂D_4 (32)

P (y=0, x, z) = P (y=1, x, z) - $\boldsymbol{G}$ on ∂D_1 and ∂D_2 (33)

u (y=0, x, z)•$\boldsymbol{n_1}$ = -u (y=1, x, z)•$\boldsymbol{n_2}$ on ∂D_1 and ∂D_2 (34)

P (y, x, z=0) = P (y, x, z=1)   on ∂D_5 and ∂D_6 (35)

u (y, x, z=0)•$\boldsymbol{n_5}$ = -u (y, x, z=1)•$\boldsymbol{n_6}$ on ∂D_6 and ∂D_6 (36)

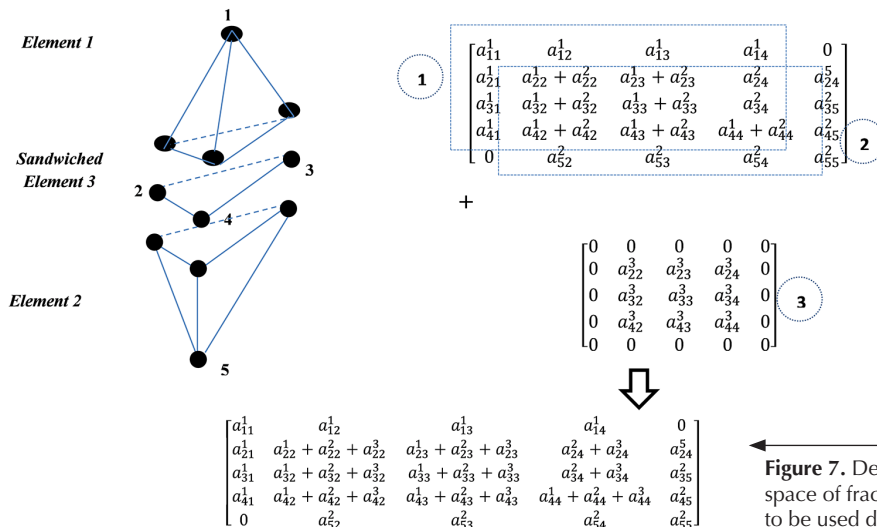where $\boldsymbol{n}$ is the outward normal vector at the boundaries, and $\boldsymbol{G}$ is the pressure gradient. The rest of permeability-tensor elements can be calculated by specifying the same boundary conditions as above-mentioned, but in the opposite directions.

The effective permeability of fractured reservoir has been calculated by using finite element technique. Each fracture is represented as a sandwiched two dimensional element (triangular) between three dimensional elements (tetrahedral) representing the matrix porous medium as shown in Figure 7.

Single phase steady state fluid-flow in matrix can be written as follows.

$$\nabla \cdot \left(\frac{\bar{\bar{k}}}{\mu} \cdot \nabla p \right) + Q_H = 0.0 \qquad (37)$$

$$v = -\left(\frac{\bar{\bar{k}}}{\mu} \nabla p \right) \qquad (38)$$

Figure 7. Description of how the whole matrix for 3D space of fractures and rock matrix elements constructed to be used during the simulation process.

where $\bar{\bar{k}}$ is a full permeability tensor, μ is the fluid viscosity, Q_H is fluid source/sink term which represents the fluid exchange between matrix and fracture, or fluid extraction (injection) from the wellbore. Fluid-flow in a single fracture is also expressed as follows:

$$\bar{\nabla} \cdot \left(\frac{k_f}{\mu} \nabla p_f \right) + q^+ q^- = 0.0 \qquad (39)$$

where q^+ and q^- are the leakage fluxes across the boundary interfaces, $\bar{\nabla}$ is the divergence operator in local coordinates system (Watanabe et al. 2010), and P_f is the pressure inside the fracture. The permeability of the fracture can be expressed by a parallel plate concept (cubic law) as shown in Eq. 40. It has been assumed that the fracture surfaces are parallel and the fluid-flow through a single discrete fracture is laminar (Snow 1969).

$$k_f = \frac{b^2}{12} \qquad (40)$$

where b is the fracture aperture, and k_f is the fracture permeability.

The weighted-residual method is then used to derive the weak formulation of the governing equation of fluid-flow through a fractured system, and the standard Galerkin method was applied to discretise the weak forms with appropriate boundary conditions (Zimmerman and Bodvarsson 1996, Woodbury and Zhang 2001).

Equations. (37) and (39) are written separately for the matrix and fractures. The matrix is discretised using 3D elements and fractures are discretised by using 2D elements. If *CFEQ* represents the control flow equations (37) and (39), the integral form of the flow equations for discrete fracture model can be written as

$$\iint_\Omega \text{CFEQ d}\Omega = \iint_{\Omega_m} \text{CFEQ d}\Omega_m + b \times \iint_{\Omega_f} \text{CFEQ d}\bar{\Omega}_f \qquad (41)$$

where $\bar{\Omega}_f$ represents the fracture part of the domain as a 2D entity, and Ω_m represents matrix domain and Ω is the entire domain. 2D integral fracture equation is multiplied by the fracture aperture b for consistency of the integral form.

The finite element formulation of the governing equation for hydraulic process in matrix and fracture can be written in the matrix form as:

$$\left[\bar{\bar{M}} \right] \left[\overrightarrow{\Delta p} \right] = \vec{f} \qquad (42)$$

$$\bar{\bar{M}} = \overline{\overline{M_1^m}} + \overline{\overline{M_2^f}} \qquad (43)$$

$$\bar{\bar{M}} = \int_\Omega \nabla N_p^{m^T} \frac{k}{\mu} \nabla N_p^m \, d\Omega +$$

$$\int_\Gamma \nabla N_p^{f^T} \left(\frac{b \times k}{\mu} \right) \nabla N_p^f \, d\Gamma \qquad (44)$$

$$\vec{f} = -\int_\Gamma N_p^{m^T} Q_H \, d\Gamma - \overline{\overline{M_1^m}} \overrightarrow{P}^{i-1^m} -$$

$$\overline{\overline{M_2^f}} \overrightarrow{P}^{i-1^f} - \int_\Gamma N_p^{f^T} Q_H \, d\Gamma \qquad (45)$$

where N is the corresponding shape function for the matrix and fracture elements and, and is a domain boundary.

After using these equations for pressure calculations, the average velocity for each reservoir block in x, y and z directions can be calculated by using Eq. (46-48) as:

$$\langle v_x \rangle = - \int_{\partial D_3} v.n_3 \, dx \ dz \tag{46}$$

$$\langle v_y \rangle = - \int_{\partial D_1} v.n_1 \, dy \ dz \tag{47}$$

$$\langle v_z \rangle = - \int_{\partial D_5} v.n_5 \, dx \ dy \tag{48}$$

Full permeability tensor components can be obtained as mentioned before by using Eqs. (28-30).

Model Validation

To validate the numerical model, a sugar-cube reservoir has been created using an in-house 3D mesh generator code with two set of orthogonal vertical fractures having the same dip angle and different azimuth. An equal fracture spacing of 250 m is assumed with a vertical well at the centre of the model penetrating the whole reservoir thickness .Horizontal fractures are ignored as they are usually not observed below moderate depth, so only vertical fractures are considered. Properties of the fractures, matrix and stress values are presented in Table (1). A single-phase draw-down test is performed for 3,500 days at a constant production rate of 5,000 bbl/day simulated numerically using a discrete-fracture approach.
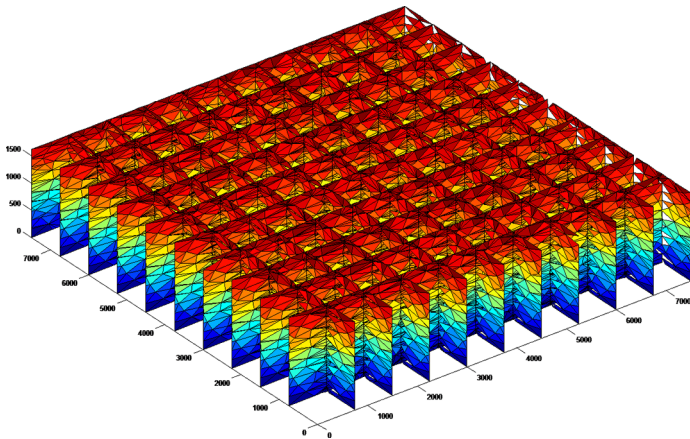
Figure 8. Stressed sugar cube model with a two set of orthogonal vertical fractures and a vertical well penetrating the model from top to the bottom at the centre.

The pressure response at the wellbore was compared against an analytical pressure-transient solution introduced by (Warren and Root 1963) for dual-porosity model.

In Figure 9 the simulated and the actual pressure change and pressure derivatives are p[resented. The pressure derivative curve is like a bell shaped between 20 hr to 1000 hr, indicating a transition flow period. In this flow period the matrix starts to feed the fractures network by fluid. During this period the fluid production at the wellbore is very low and pressure starts to drop slowly. The

Table 1. Input data for a sugar cube model used in a numerical simulation validation process.

| Reservoir dimensions	7500m x 7500m x1620 m
Fracture spacing	250m
Matrix permeability	0.01mD
Matrix porosity	0.01
Fracture permeability	1000mD
Wellbore storage	0 bbl/psi^{-1}
Initial reservoir pressure	10,000psia
Fluid viscosity	0.2cp
Fluid compressibility	22.4E-06psi^{-1}
Horizontal stresses	9000psi
Vertical stress	12000psi

dip of this bell shaped is controlled by the value of storativity ratio (ω). As the (ω) gets smaller, the dip gets deeper and starts earlier.

The horizontal portion of the pressure derivative curve from 1000 hr to 40,000 hr indicates the end of transition period and start of the composite system flow. This flow period is controlled by the value of interporosity flow coefficient (λ). The unit slope of pressure derivative curve between 10,000 hr to 100,000 hr indicates pseudo steady-state condition for the entire reservoir volume. By using this flow period, a reservoir volume and shape can be calculated. At early time response for idealized dual-porosity transient behaviour with a very low wellbore storage effects, a first radial flow regime is expected to appear before starting of transition flow period. This radial flow regime is governed by the flow only inside the fractures. As shown in Figure 9, there is a good agreement between the results of this study with that of the analytical solution.
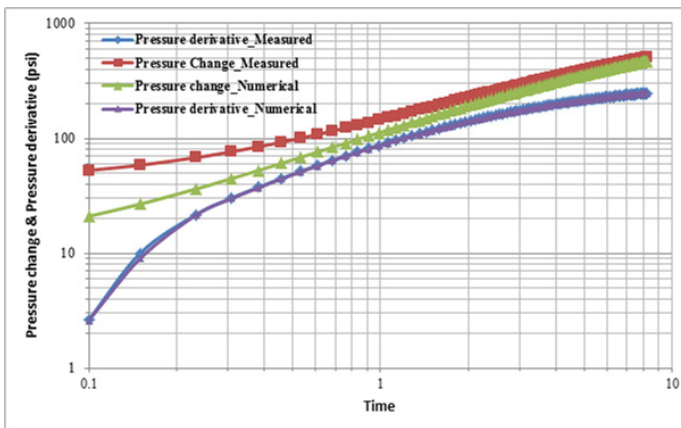
Case Study

Despite the presence of multiple fractures in various sections of the Habanero geothermal field, the vast majority of fluid flow occurs over a short section of intensely fractured zone referred to as the "Main Fracture" (Bendall et al.). First the poro elastic numerical model is used to simulate pressure change pressure derivatives for given pressure drawdown situation. The simulated pressure draw-down are then compared with that of the field data. Following this an analysis of hot water production is performed for three well configurations, Habanero #1, Habanero #2 and Habanero #3. Habanero #1 is the injection well and Habanero well #2 & #3 are the production wells. Well location and distance between wells are chosen based on the Habanero geothermal system. This information is used to study hot water production rate, produced fluid temperature, pressure- and velocity profile.
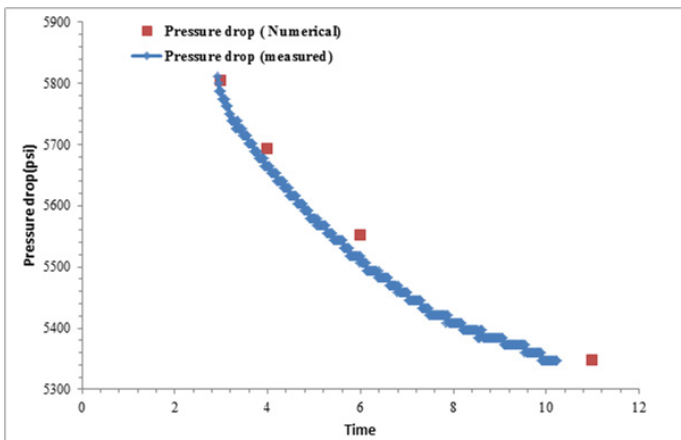
Pressure drawdown in the production well Habanero #2 versus time and its derivative are presented in Figures 10 & 11. The results of this study are also compared with that from Habanero geothermal reservoir. As can be seen in Figure 14, the pressure profile from both studies exhibit the same pattern with the exception that, at the early times, the change in pressures are shifted by about half a cycle from that of the measured data. This shift at early times is due to the lack of information on reservoir properties. It is, however, noteworthy that the pressure derivatives obtained based on the current study are in a good agreement with that of the measured data from the Habanero geothermal reservoir.
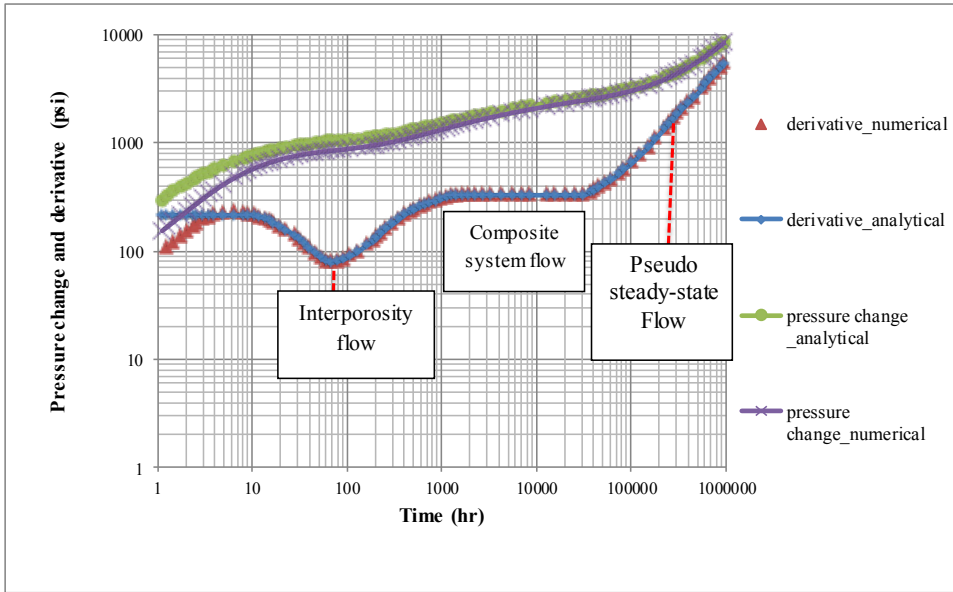
Figure 9. Pressure transient response of the sugar cube model generated by the developed model in the current study against that of generated with the dual porosity model.
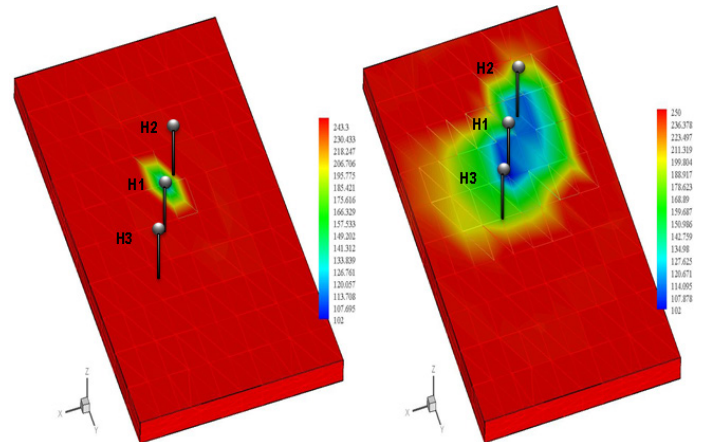
Rock temperature distribution of Habanero reservoir after 1 year and 10 years of cold fluid circulation are presented in Figure 12. As shown in the figure, the thermal breakthrough occurs at Habanero #2 after 10 years of cold water injection with the fluid temperature of 100 °C. The significantly high rate of reservoir matrix cooling shows that that the temperature draw down is controlled by convective heat transfer.

The produced fluid temperature versus time for the Habanero #2 well is shown in Figure 13. As shown in the figure, the produced fluid temperature declines at a significantly high rate until about 2 years of hot water production after which the produced fluid temperature decreases at a much slower rate. This is attributed to the effect of reservoir pressurization which opens up fluid paths in parts of the reservoir which was not connected previously.
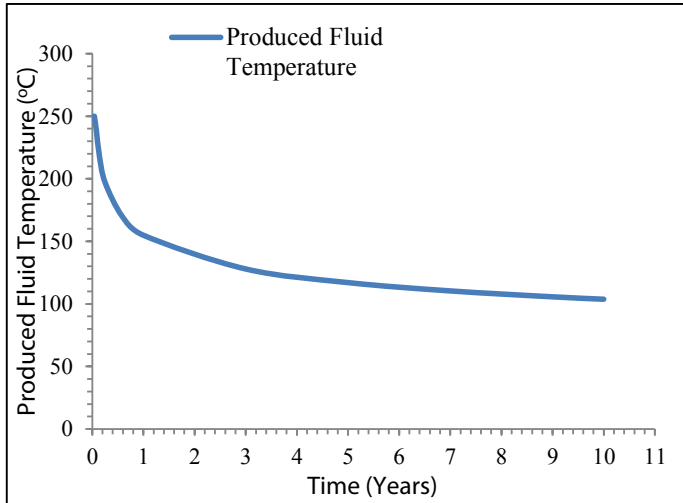

Figure 10. Log-log plot of pressure derivative and pressure change of a draw down test conducted in Habanero #2 well.

Figure 12. Rock matrix temperature distribution in °C in Habanero reservoir with σ_H = 62 MPa and σ_h = 58.6MPa, σ_v = 82.7 MPa, Pinj = 49.6 MPa, Δp = 21.37 MPa, T_{inj} = 100 °C, Ti = 250 °C and p_i = 35.16 MPa after 1 year (left), 10 years (right).

In another word, at the beginning of the hot water production few fractures participated in the cold fluid circulation, therefore the produced fluid temperature decreases rapidly during this period. As the time passes, a large number of fractures are contributing to the fluid flow which increases heat transfer from rock to fluid thus arresting sharp decline in produced fluid temperature over longer term.

The effect of fluid injection on reservoir pressure and fluid velocity profiles after one year and 10 years of hot water production are presented in Figures 14 & 15. As shown in figures (left), after one year of cold fluid circulation, the reservoir pressure and fluid velocity are significantly high around the injection well (H-1). With continuous fluid circulation until 10 years (right) pressure and fluid velocity reach to a quasi-steady state and the variation of pore pressure and fluid velocity remain roughly constant.

Figure 11. Plot of a history drawdown test of Habanero #2 well and also the pressure drop resulted from numerical model.

Figure 13. Produced fluid temperature at late time (>7 years). The injector bottomhole pressure, p_{inj} is kept constant at 48.95 MPa, with an injector–producer pressure drop Δp of 21.37 MPa. Cold water injected at T_{inj} = 80 °C. Initial reservoir temperature Ti = 250 °C and initial reservoir pressure p_i = 35.16 MPa.
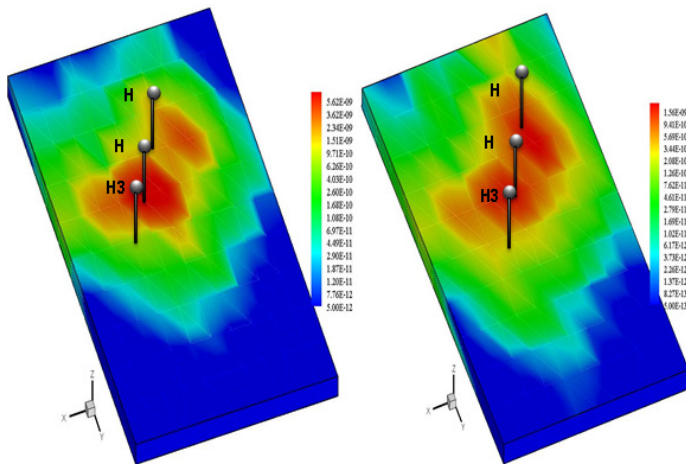
Conclusion

The 3D numerical poro-thermo-elastic model is validated using an analytical model. Next the model is used to simulate pressure derivatives and compared with that from the Habanero geothermal reservoir. The simulated results agree well with the pressure transient data, thus making the model an effective tool for characterising naturally fracture reservoirs. It has also allowed us to study changes in pressure, velocity, produced fluid temperature, production rate and matrix temperature draw-down of the reservoir for different stress condition and injection schedules. The results of this study show that the produced fluid temperature drops at a faster rate at early time and levels off with the pass of time. This can be explained by the fact that with the pass time more fractures undergo dilation process, as a result of which the circulating fluid covers larger volume of rocks away from the wellbores. Cooling of the formation matrix induces tensile thermal stresses which allow residing fractures to open and enhance permeability. This gradually increases the number of active flow paths between the injector and the producer.

Acknowledgement

The authors would like to thank Geodynamics Limited for providing the microseismic and pressure transient data of Habanero geothermal field.

Figure 14. Fluid velocity distribution in Habanero reservoir with σ_H = 62 MPa and σ_h = 58.6MPa, σ_v = 82.7 MPa, P_{inj} = 49.6 MPa, Δp = 21.37 MPa, T_{inj} = 100 °C, Ti = 250 °C and p_i = 35.16 MPa after 1 year (left), 10 years (right). Contour units in m/s.
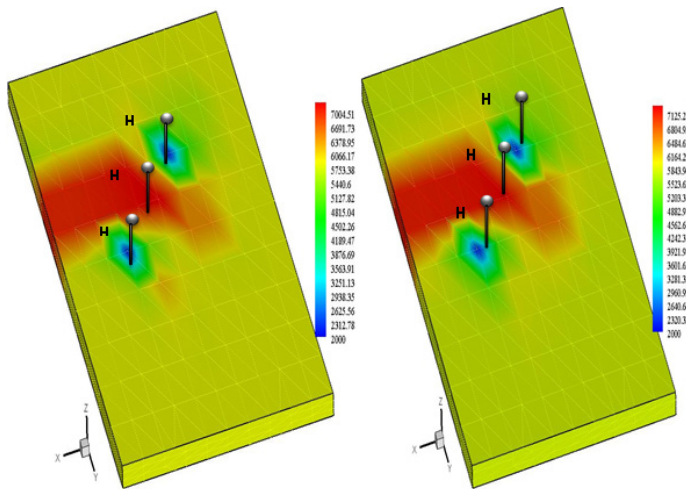
Figure 15. Pore pressure distribution in the Habanero reservoir with σ_H = 62 MPa and σ_h = 58.6MPa, σ_v = 82.7 MPa, P_{inj} = 49.6 MPa, Δp = 21.37 MPa, T_{inj} = 100 °C, Ti = 250 °C and p_i = 35.16 MPa after 1 year (left), 10 years (right). Contour units in psi.

References

Alghalandis, Y. F., P. A. Dowd and C. Xu (2013). "The RANSAC method for generating fracture networks from micro-seismic event data." *Mathematical Geosciences* 45(2): 207-224.

Barenblatt, G., I. P. Zheltov and I. Kochina (1960). "Basic concepts in the theory of seepage of homogeneous liquids in fissured rocks." *J. Appl. Math. Mech* 24(5): 1286-1303.

Barenblatt, G. I. and I. Zheltov (1960). *Basic flow equations for homogeneous fluids in naturally fractured rocks*. Dokl. Akad. Nauk.

Bathe, K. J. (1996). *Finite element procedures*, Prentice Hall.

Beckner, B. L., K. Ishimoto, S. Yamaguchi, A. Firoozabadi and K. Aziz (1987). Imbibition-Dominated Matrix-Fracture Fluid Transfer in Dual Porosity Simulators. *SPE Annual Technical Conference and Exhibition*. Dallas, Texas, 1987 Copyright 1987, Society of Petroleum Engineers.

Bendall, B., R. Hogarth, H. Holl, A. McMahon, A. Larking and P. Reid "Australian Experiences in EGS Permeability Enhancement–A Review of 3 Case Studies."

Doonechaly, N. G., S. S. Rahman and A. Kotousov (2013). "A New Approach to Hydraulic Stimulation of Geothermal Reservoirs by Roughness Induced Fracture Opening."

Gholizadeh Doonechaly, N. and S. S. Rahman (2012). "3D hybrid tectono-stochastic modeling of naturally fractured reservoir: Application of finite element method and stochastic simulation technique." *Tectonophysics* 541–543(0): 43-56.

Gholizadeh Doonechaly, N., S. S. Rahman and A. Kotousov (2012). "An Innovative Stimulation Technology for Permeability Enhancement in Enhanced Geothermal System--Fully Coupled Thermo-Poroelastic Numerical Approach." *36th Geothermal Resources Council Transactions*.

Gholizadeh Doonechaly, N., S. S. Rahman and A. Kotousov (2012). "A Realistic Assessment of Recoverable Thermal Energy from Australian Geothermal Reservoirs: A Simulation Study." *Proceedings of the 2012 Australian Geothermal Energy Conference*

Koh, J., N. Gholizadeh Doonechaly, A. R. Shaik, S. S. Rahman and L. Mortimer (2010). "Reservoir characterisation and numerical modelling to reduce project risk and maximise the chance of success. An example of how to design a stimulation program and assess fluid production from the Soultz geothermal field, France." *Australian Geothermal Conference*.

Koh, J., H. Roshan and S. S. Rahman (2011). "A numerical study on the long term thermo-poroelastic effects of cold water injection into naturally fractured geothermal reservoirs." *Computers and Geotechnics* 38(5): 669-682.

March, W. B., P. Ram and A. G. Gray (2010). *Fast euclidean minimum spanning tree: algorithm, analysis, and applications*. Proceedings of the 16th ACM SIGKDD international conference on Knowledge discovery and data mining, ACM.

Nelson, P. P. and S. E. Laubach (1994). *Rock mechanics models and measurements: challenges from industry ; proceedings of the 1st North American Rock Mechanics Symposium, the University of Texas at Austin, 1-3 June 1994*, A.A. Balkema.

Warpinski, N., S. Wolhart and C. Wright (2004). "Analysis and prediction of microseismicity induced by hydraulic fracturing." *SPE Journal* 9(01): 24-33.

Warren, J. E. and P. J. Root (1963). "The behavior of naturally fractured reservoirs." *SPE Journal* 3(3): 245-255.

Watanabe, N. (2012). *Finite element method for coupled thermo-hydro-mechanical processes in discretely fractured and non-fractured porous media*, PhD Thesis, Technische Universität Dresden, Chair of Applied Environmental System Analysis, Helmholtz Centre for Environmental Research UFZ, Department of Environmental Informatics.

Watanabe, N., W. Wang, C. McDermott, T. Taniguchi and O. Kolditz (2010). "Uncertainty analysis of thermo-hydro-mechanical coupled processes in heterogeneous porous media." *Computational Mechanics* 45(4): 263-280.

Woodbury, A. and K. Zhang (2001). "Lanczos method for the solution of groundwater flow in discretely fractured porous media." *Advances in Water Resources* 24(6): 621-630.

Zienkiewicz, O. C. T., R L; Nithiarasu, P; (2000). "The Finite Element Method for Fluid Dynamics, Sixth Edition."

Zimmerman, R. and G. Bodvarsson (1996). "Hydraulic conductivity of rock fractures." *Transport in Porous Media* 23(1): 1-30.